


# Influence of static correlation on the magnon dynamics of an itinerant ferromagnet with competing exchange interactions: First-principles study of MnBi

Thorbjørn Skovhus<sup>1</sup>, Thomas Olsen<sup>1,\*</sup> and Henrik M. Rønnow<sup>2</sup>

<sup>1</sup>CAMD, Department of Physics, Technical University of Denmark, 2800 Kgs. Lyngby, Denmark

<sup>2</sup>LQM, Institute of Physics, École Polytechnique Fédérale de Lausanne, CH-1015 Lausanne, Switzerland

 (Received 14 October 2021; revised 11 February 2022; accepted 29 March 2022; published 4 May 2022)

We present first-principles calculations of the dynamic susceptibility in strained and doped ferromagnetic MnBi using time-dependent density functional theory. In spite of being a metal, MnBi exhibits signatures of strong correlation and a proper description in the framework of density functional theory requires Hubbard corrections to the Mn  $d$  orbitals. To permit calculations of the dynamic susceptibility with Hubbard corrections applied to the ground-state electronic structure, we use a consistent rescaling of the exchange-correlation kernel maintaining the delicate balance between the magnon dispersion and the Stoner continuum. We find excellent agreement with the experimentally observed magnon dispersion for pristine MnBi and show that the material undergoes a phase transition to helical order under application of either doping or strain. The presented methodology paves the way for future linear response time-dependent density functional theory studies of magnetic phase transitions, also for the wide range of materials with pronounced static correlation effects that are not accounted for at the local density approximation level.

DOI: [10.1103/PhysRevMaterials.6.054402](https://doi.org/10.1103/PhysRevMaterials.6.054402)

## I. INTRODUCTION

MnBi has been proposed as a promising alternative to permanent magnets based on rare-earth elements [1–3]. This is primarily due to the large spontaneous magnetization at room temperature [4], strong uniaxial magnetic anisotropy [5], and the abundance of its constituent elements [6]. Moreover, it exhibits an extraordinarily large Kerr rotation [7], which makes it an ideal candidate for magneto-optical data storage applications [8,9]. From a fundamental point of view, MnBi is an intriguing material since it can be regarded as a member of the transition metal pnictides  $AX$  ( $A = \text{V/Cr/Mn/Fe/Co/Ni}$ ,  $X = \text{P/As/Sb}$ ), which realize a wide variety of spiral magnetic orders depending on the composition, pressure, and temperature [10–12]. In particular, MnP and CrAs have recently been demonstrated to exhibit unconventional superconductivity below 1 [13] and 2 K [14], respectively. The superconducting state emerges at the critical pressure for magnetic order and has been argued to imply an unconventional mechanism for Cooper pairing associated with magnetic quantum fluctuations [14]. Thus, the microscopic origin of different spiral orders in transition metal pnictides is of high interest along with the influence of doping and strain. For example, at low temperatures MnP exhibits helical order at ambient pressure, becomes ferromagnetic at  $\sim 1$  GPa, makes a transition to a second helical phase at  $\sim 1.5$  GPa, and finally becomes paramagnetic at 6.7 GPa with a superconducting window at pressures  $6.7 < P < 8$  GPa [10]. While MnBi has not been reported to exhibit phase transitions involving helical order, a phase transition from

ferromagnetic to helical order has been observed for the isostructural MnAs upon doping with Cr [15] and it is not unlikely that a similar transition may occur for MnBi.

At room temperature, MnBi crystallizes in the hexagonal NiAs structure with space group  $P6_3/mmc$ . Upon cooling, MnBi undergoes a structural phase transition at 90 K, where the in-plane hexagonal symmetry is slightly broken and the crystal structure becomes orthorhombic (space group  $Cmcm$ ) [16]. It is ferromagnetic up to 630 K where it segregates into  $\text{Mn}_{1.08}\text{Bi}$  and Bi [17], which are both paramagnetic. The true Curie temperature is thus unknown, but the lower bound of 630 K indicates strong magnetic interactions in the material. At room temperature, MnBi exhibits a large uniaxial magnetic anisotropy along the  $c$  axis of the NiAs crystal structure. The anisotropy decreases with decreasing temperature and aligns with the  $ab$  plane of the orthorhombic phase below 90 K [16]. For thin film [18,19] and nanocrystalline [20] MnBi, it has been shown that Cr doping lowers the Curie temperature below the segregation temperature for  $\text{Mn}_{1-x}\text{Cr}_x\text{Bi}$  doping levels down to at least  $x = 0.03$ . For Cr doping in the range of 3%–15%, Curie temperatures have been recorded to lie in the 520–560 K range. Moreover, the coercivity has been shown to increase significantly by Cr doping [20], while the beneficial magneto-optical properties are retained. To our knowledge there have so far not been attempts to study the low-temperature magnetic structure of Cr-doped MnBi.

The magnon spectrum of MnBi was measured at 5 K by Williams *et al.* using inelastic neutron scattering (INS) [21]. The hexagonal phase was assumed in the analysis of results, which is likely to be a good approximation due to the strong similarity with the orthorhombic phase expected at low temperatures [21]. The magnon bandwidth is on the order of 100 meV and the spectrum was found to be gapless as

\*tolsen@fysik.dtu.dk

expected from the easy-plane anisotropy at low temperatures. It was shown that the spectrum is well reproduced by fitting to an isotropic Heisenberg model with six exchange parameters. While such a fit may not be unique, the nearest-neighbor interaction was unambiguously shown to be antiferromagnetic having the largest magnitude of all interactions. The inherent magnetic frustration thus makes it highly plausible that a magnetic phase transition may be induced by external strain or doping, which will inevitably influence the individual exchange parameters differently.

From a computational perspective, the magnon spectrum of magnetic materials can be accessed at various levels of theory. Typically, a theoretical treatment will take one of the following three starting points: a mapping to a model Hamiltonian, an adiabatic approximation separating the transverse magnetic fluctuations from the faster electronic (longitudinal) degrees of freedom, or an *ab initio* treatment of the full dynamic transverse magnetic susceptibility. In the following, these three starting points will be referred to as model-based approaches, adiabatic approaches, and theoretical magnon spectroscopy, respectively. However, this classification is not unique and approaches with different starting points may in practice end up in equivalent overall treatments.

The simplest model-based approach is to assume a Heisenberg model and extract exchange parameters in a total energy mapping analysis within the framework of density functional theory (DFT) [22–24]. This will directly yield the spin-wave energy dispersion in the noninteracting magnon approximation to the model, but will not elucidate itinerant electron effects such as the line-shape broadening (Landau damping) from the spectral overlap with the single-particle excitation continuum in metals (Stoner continuum). For materials with a collinear ground state it is possible to calculate the nearest-neighbor exchange interaction of the quantum mechanical Heisenberg model using an energy mapping without spin-orbit effects [24]. In the general case, however, there may not necessarily exist a meaningful energy mapping from a set of collinear magnetic configurations within DFT to the quantum mechanical Heisenberg model and one has to resort to a classical model of the magnetic interactions. Furthermore, any approach based on the Heisenberg model relies on the magnons being well described in terms of localized spins. This assumption becomes somewhat dubious for metallic systems, although it is often still possible to fit spin-wave spectra to a Heisenberg model if enough exchange parameters are included in the fit [25]. For this reason, it is usually preferable to compute the Heisenberg exchange parameters directly from the magnetic force theorem (MFT) [26–28] in the case of metals. Within the MFT framework, the Heisenberg exchange can be calculated in reciprocal space, allowing access to interactions on all length scales without any fundamental additional computational complexity.

In the adiabatic approach, it is assumed that the time-dependent magnetization  $\mathbf{m}(\mathbf{r}, t)$ , which describes the magnon dynamics, can be treated as a classical variable on the timescale of the transverse magnetic fluctuations. This assumption implies that the underlying electronic degrees of freedom always should minimize the system energy given  $\mathbf{m}(\mathbf{r}, t)$  on this timescale. Within such an approximation, the magnon dynamics is governed by a classical equation of

motion (EOM) for  $\mathbf{m}(\mathbf{r}, t)$ , from which the magnon dispersion may be extracted [29–31]. The material-dependent parameters in the EOM can be computed based on a number of frozen magnon configurations generated within constrained DFT. However, it is not trivial to treat an arbitrary noncollinear magnetic structure consistently, and the frozen magnons have to be generated with care in order to reliably compute the magnon dispersion [32,33]. Although the adiabatic magnon EOM can be diagonalized in reciprocal space without any constraints on the spatial dependence of the magnetization [29,32], it is often assumed that the magnetization can be represented in terms of localized (atomic) sites of volumes  $V_i$  within which the direction of the magnetization is constant [30,33,34]. Within such a truncation of the spatial representation, the adiabatic approximation essentially reduces the magnon dynamics to those of the classical Heisenberg model [34,35]. Thus, when relying on the atomic sphere approximation or any similar spirited spatial partitioning of the magnetization, the adiabatic (frozen magnon) approach is essentially equivalent in nature to the energy mapping and MFT approaches, despite that the theoretical starting points and computational details may differ quite substantially. For this reason, all of the above approaches may be viewed as adiabatic, and they all share the characteristic that the magnon interaction with the Stoner continuum is neglected and that only the spin-wave stiffness of itinerant ferromagnets can be treated exactly [36,37].

In order to appropriately capture the effects of the Stoner continuum on the magnon dispersion of itinerant ferromagnets, one needs either to map the problem onto a model accounting for the electronic degrees of freedom (e.g., a Hubbard model) or move on to the third approach, theoretical magnon spectroscopy. This approach relies on many-body perturbation theory (MBPT) or time-dependent density functional theory (TDDFT) to compute the full spectral function for the transverse magnetic excitations, which directly facilitates comparison and analysis of experimental results. In this work, we apply the linear response TDDFT (LR-TDDFT) method to compute the magnon dispersion of MnBi. Our methodology includes the renormalization effects of the Stoner continuum on the magnon dispersion, but does not aim to provide the reduced magnon lifetimes due to Landau damping as the lifetimes are above the current numerical resolution of our computational implementation. The framework of TDDFT in general [38] and LR-TDDFT [39] in particular have previously been successfully applied to extract magnon dispersion relations for several simple itinerant ferromagnets [40–47], just as it is the case for MBPT [48–52]. While the framework itself is formally exact, LR-TDDFT in practice relies on approximations to the exchange-correlation kernel, such as the adiabatic local density approximation (ALDA). The accuracy of the approximation is strongly dependent on the system at hand. For example, ALDA LR-TDDFT captures the magnon spectrum of bcc Fe and hcp Co rather accurately, whereas the bandwidth of the magnon spectrum of fcc Ni is overestimated by a factor of 2 [41,43,44,47]. The main reason for the inaccuracy is likely related to the inability of ALDA to correct for the Kohn-Sham exchange splitting, which is overestimated in LDA [50].

In the context of ground-state DFT, the disagreement between the Kohn-Sham spectrum and the quasiparticle

spectrum may often be alleviated by the DFT +  $U$  approach [53–55] where an onsite Hubbard repulsion is added, which tends to localize orbitals as well as increase band gaps and exchange splittings. In particular, Antropov *et al.* [56] have shown that a Hubbard correction is crucial in order to describe the ground-state magnetic moments and the temperature-dependent magnetic anisotropy correctly in MnBi. Similarly, a Hubbard correction is also needed to reach an appropriate description of the structural properties of MnBi [57]. However, in the context of LR-TDDFT it is not obvious how to include the Hubbard correction at the level of the exchange-correlation kernel, which introduces a mismatch between the kernel and the orbitals. This has severe consequences for the calculations since the delicate balance between the magnon spectrum and single-particle excitations is lost, leading to a gross violation of the Goldstone theorem in the combination of DFT +  $U$  and ALDA LR-TDDFT.

To remedy this violation, we apply a scalar rescaling of the exchange-correlation kernel, eliminating the mismatch between single-particle Stoner spectrum and magnon spectrum. The rescaling is fixed by the requirement of a gapless acoustic magnon mode and does not introduce any new free parameters apart from the ground-state Hubbard correction. A scalar rescaling of the effective (screened) Coulomb interaction has also previously been adopted for theoretical magnon spectroscopy within MBPT [50,51], where it is prohibitively difficult to treat the effective interaction at full self-consistency with the single-particle Stoner continuum [58]. In this context, it has also been investigated whether a Hubbard correction (with rescaling of the effective interaction) could improve the faulty LDA magnon dispersion of fcc Ni, with mixed success [50]. In this work, it is shown that the experimentally measured magnon spectrum of MnBi is accurately captured within  $\lambda$ ALDA +  $U$  LR-TDDFT, whereas the neglect of Hubbard corrections leads to an overestimation of the optical magnon frequencies by at least a factor of 2. In this way, it is demonstrated that static correlation effects beyond the LDA are essential to include in order to correctly capture the inherent magnetic frustration in MnBi, and that a ground-state Hubbard correction is a viable method in this regard. In particular, the correction strengthens the out-of-plane antiferromagnetic exchange interaction, and when artificially increasing the Hubbard correction beyond the experimental match, MnBi is imposed a phase transition to helical order. In addition, we demonstrate that MnBi undergoes a similar phase transition upon the introduction of either hole doping (as one would expect in a Cr alloy) or uniaxial compressive strain in the out-of-plane direction.

The paper is organized as follows. In Sec. II we outline the theoretical concepts underlying the LR-TDDFT framework for theoretical magnon spectroscopy. In Sec. III we show how the Hubbard correction is included and how we determine the rescaling of the exchange-correlation kernel, which is required when combining LDA +  $U$  with ALDA LR-TDDFT. In addition, we also supply the computational details. In Sec. IV we present the results of our study, including the effect of static correlations on ground- and excited-state properties of pristine MnBi as well as the effect of hole doping and uniaxial compressive strain on the magnon dynamics. Finally, in Sec. V we discuss how the results fit in as another piece in

the puzzle of complex magnetic phases in the transition metal pnictide family and in Sec. VI we summarize our conclusions.

## II. THEORY

### A. Transverse magnetic susceptibility

As exploited experimentally in inelastic neutron scattering and similar spectroscopic techniques, one may probe the fundamental excitations of a material by studying its response to external perturbations. In a nonrelativistic treatment, the linear order response in the transverse magnetic degrees of freedom can be fully characterized by a single response function, namely, the transverse magnetic susceptibility. The susceptibility is given by the *Kubo formula*

$$\chi^{+-}(\mathbf{r}, \mathbf{r}', t - t') = -\frac{i}{\hbar} \theta(t - t') \langle [\hat{n}_0^+(\mathbf{r}, t), \hat{n}_0^-(\mathbf{r}', t')] \rangle_0, \quad (1)$$

where  $\langle \cdot \rangle_0$  is the expectation value with respect to the ground state,  $\theta(t - t')$  is the step function, and  $\hat{n}^\pm$  are the spin-raising and spin-lowering density operators, respectively:

$$\hat{n}^+(\mathbf{r}) = \hat{\psi}_\uparrow^\dagger(\mathbf{r})\hat{\psi}_\downarrow(\mathbf{r}), \quad \hat{n}^-(\mathbf{r}) = \hat{\psi}_\downarrow^\dagger(\mathbf{r})\hat{\psi}_\uparrow(\mathbf{r}). \quad (2)$$

In Eq. (1), the operators carry the time dependence of the interaction picture  $\hat{n}_0^\pm(\mathbf{r}, t) \equiv e^{i\hat{H}_0 t/\hbar} \hat{n}^\pm(\mathbf{r}) e^{-i\hat{H}_0 t/\hbar}$ , where  $\hat{H}_0$  is the Hamiltonian of the unperturbed system, which in the case of MnBi has a ferromagnetic ground state. Furthermore, one may interchange the + and - indices in Eq. (1) to define the susceptibility  $\chi^{-+}$ , but thanks to the relation  $\chi^{-+}(\mathbf{r}, \mathbf{r}', -\omega) = \chi^{+-*}(\mathbf{r}, \mathbf{r}', \omega)$ , it is sufficient to consider only  $\chi^{+-}$ . Beyond the nonrelativistic limit, one in general needs to consider the full four-component susceptibility tensor in order to characterize the magnetic modes of excitation [47]. However, down to the experimental resolution of 6 meV, the available INS spectrum of MnBi does not exhibit any effects of the magnetic anisotropy [21], why such effects are neglected in this study as well.

From the dissipative (antisymmetric) part of the transverse magnetic susceptibility, one may extract the spectrum of induced excitations [47]:

$$S^{+-}(\mathbf{r}, \mathbf{r}', \omega) = -\frac{1}{2\pi i} [\chi^{+-}(\mathbf{r}, \mathbf{r}', \omega) - \chi^{-+}(\mathbf{r}', \mathbf{r}, -\omega)]. \quad (3)$$

For a ferromagnet (assumed spin-polarized along the  $z$  direction), this spectrum determines the energy dissipation from weak perturbations in the transverse magnetic field  $B_{\text{ext}}^{x/y}(\mathbf{r}, t)$ . Furthermore,  $S^{+-}(\mathbf{r}, \mathbf{r}', \omega)$  constitutes a spectral function for the excited states which differ by a single unit of spin angular momentum compared to the ground state. In this way, one may use various spectroscopic techniques to extract  $S^{+-}(\mathbf{r}, \mathbf{r}', \omega)$ , permitting direct access to the transverse magnetic excitations of the system. Alternatively,  $S^{+-}(\mathbf{r}, \mathbf{r}', \omega)$  can be computed by theoretical spectroscopy techniques, providing significant aid to the interpretation of measurements. More importantly, calculations of the transverse susceptibility allow one to rapidly scrutinize the effect of material modifications such as strain and doping, which may be time consuming and costly to investigate experimentally.

### B. Computing the transverse magnetic susceptibility within LR-TDDFT

As a consequence of the Runge-Gross theorem [38], the time-dependent electronic structure of any material may be characterized in terms of an auxiliary Kohn-Sham system of noninteracting electrons where the electronic Coulomb repulsion is replaced by an effective (electromagnetic) potential. The susceptibility of the Kohn-Sham system can be evaluated using only quantities from a routine ground-state DFT calculation [59–62]

$$\chi_{\text{KS}}^{+-}(\mathbf{r}, \mathbf{r}', \omega) = \lim_{\eta \rightarrow 0^+} \frac{1}{N_k^2} \sum_{nk} \sum_{mk'} (f_{nk\uparrow} - f_{mk'\downarrow}) \times \frac{\psi_{nk\uparrow}^*(\mathbf{r}) \psi_{mk'\downarrow}(\mathbf{r}) \psi_{mk'\downarrow}^*(\mathbf{r}') \psi_{nk\uparrow}(\mathbf{r}')}{\hbar\omega - (\epsilon_{mk'\downarrow} - \epsilon_{nk\uparrow}) + i\hbar\eta}, \quad (4)$$

where  $N_k$  is the number of  $k$  points,  $\psi_{nk_s}(\mathbf{r})$  the Kohn-Sham orbital of band index  $n$ ,  $k$  point  $\mathbf{k}$ , and spin  $s$ ,  $f_{nk_s}$  the ground-state occupancy, and  $\epsilon_{nk_s}$  the single-particle energy. In the adiabatic local density approximation (ALDA), the transverse magnetic susceptibility is directly related to the corresponding Kohn-Sham susceptibility through a single Dyson equation [39]

$$\chi^{+-}(\mathbf{r}, \mathbf{r}', \omega) = \chi_{\text{KS}}^{+-}(\mathbf{r}, \mathbf{r}', \omega) + \int d\mathbf{r}_1 \times \chi_{\text{KS}}^{+-}(\mathbf{r}, \mathbf{r}_1, \omega) f_{\text{LDA}}^{+-}(\mathbf{r}_1) \chi^{+-}(\mathbf{r}_1, \mathbf{r}', \omega), \quad (5)$$

where  $f_{\text{LDA}}^{+-}(\mathbf{r}_1) = 2W_{\text{xc,LDA}}^z(\mathbf{r})/n^z(\mathbf{r})$  is the transverse LDA kernel. Similar to the Kohn-Sham susceptibility, the kernel is given solely in terms of ground-state quantities, namely, the magnetic contribution to the LDA exchange-correlation potential  $W_{\text{xc,LDA}}^z(\mathbf{r})$  (equal to the effective magnetic field up to a factor of  $\mu_B$ ), and the spin-polarization density  $n^z(\mathbf{r})$ . In this way, one can compute the many-body susceptibility of a given material within LR-TDDFT by computing  $\chi_{\text{KS}}^{+-}(\mathbf{r}, \mathbf{r}', \omega)$  and  $f_{\text{LDA}}^{+-}(\mathbf{r})$  for the LDA ground state and inverting the Dyson equation (5) within a suitable basis.

### C. Magnons and the plane-wave susceptibility

For periodic crystals (where  $\hat{H}_0$  is invariant under lattice transformations  $\hat{T}_{\mathbf{R}}$ ), one may characterize the transverse magnetic response in terms of the plane-wave susceptibility

$$\chi_{\text{GG}'}^{+-}(\mathbf{q}, \omega) = \iint \frac{d\mathbf{r} d\mathbf{r}'}{\Omega} e^{-i(\mathbf{G}+\mathbf{q})\cdot\mathbf{r}} \chi^{+-}(\mathbf{r}, \mathbf{r}', \omega) e^{i(\mathbf{G}'+\mathbf{q})\cdot\mathbf{r}'}, \quad (6)$$

where  $\Omega$  is the crystal volume,  $\mathbf{G}$  and  $\mathbf{G}'$  are reciprocal lattice vectors, and  $\mathbf{q}$  is a wave vector within the first Brillouin zone (BZ). The plane-wave susceptibility determines the coefficients for the linear order plane-wave response  $\propto e^{i(\mathbf{G}+\mathbf{q})\cdot\mathbf{r}-i\omega t}$  to an external plane-wave perturbation  $\propto e^{i(\mathbf{G}'+\mathbf{q})\cdot\mathbf{r}-i\omega t}$ , a response which is diagonal in the reduced wave vector  $\mathbf{q}$ , thanks to the periodicity of the crystal.

In full analogy with Eq. (3), one can compute the plane-wave spectrum of induced excitations [47]:

$$S_{\text{GG}'}^{+-}(\mathbf{q}, \omega) = -\frac{1}{2\pi i} [\chi_{\text{GG}'}^{+-}(\mathbf{q}, \omega) - \chi_{-\mathbf{G}'-\mathbf{G}}^{-+}(-\mathbf{q}, -\omega)]. \quad (7)$$

This spectrum can be decomposed into contributions from spin-lowering and spin-raising excitations encoded in the spectral functions  $A_{\text{GG}'}^{+-}(\mathbf{q}, \omega)$  and  $A_{\text{GG}'}^{-+}(\mathbf{q}, \omega)$ , respectively:

$$S_{\text{GG}'}^{+-}(\mathbf{q}, \omega) = A_{\text{GG}'}^{+-}(\mathbf{q}, \omega) - A_{-\mathbf{G}'-\mathbf{G}}^{-+}(-\mathbf{q}, -\omega). \quad (8)$$

Both of these spectral functions have peaks at frequencies  $\hbar\omega = E_\alpha - E_0$  corresponding to the transition energies between the excited states  $|\alpha\rangle$  and the ground state  $|\alpha_0\rangle$ . The contribution from each excited state is weighted by the reciprocal space pair densities  $n_{\alpha\alpha'}^j(\mathbf{G} + \mathbf{q})$ :

$$A_{\text{GG}'}^{jk}(\mathbf{q}, \omega) = \frac{1}{\Omega} \sum_{\alpha \neq \alpha_0} n_{\alpha\alpha'}^j(\mathbf{G} + \mathbf{q}) n_{\alpha_0}^k(-\mathbf{G}' - \mathbf{q}) \times \delta(\hbar\omega - (E_\alpha - E_0)), \quad (9)$$

where  $\delta(\hbar\omega - \Delta E)$  denotes the Dirac delta function. The reciprocal space pair densities are Fourier transforms of the real-space pair densities  $n_{\alpha\alpha'}^j(\mathbf{r}) = \langle \alpha | \hat{n}^j(\mathbf{r}) | \alpha' \rangle$ . As the effect of the spin-lowering and spin-raising operators is to remove a spin-up or a spin-down electron at the position  $\mathbf{r}$ , respectively, and replace it with an electron of the opposite spin, the  $A^{+-}$  and  $A^{-+}$  spectral functions include only excited states for which the spin angular momentum has been either lowered or raised by a single unit compared to the ground state. Furthermore, the reciprocal space pair densities are only nonzero for excited states which differ in crystal momentum by  $\hbar\mathbf{q}$  compared to the ground state. In this way,  $A_{\text{GG}'}^{+-}(\mathbf{q}, \omega)$  and  $A_{\text{GG}'}^{-+}(\mathbf{q}, \omega)$  encode quasiparticle excitations of energy  $\hbar\omega$  and crystal momentum  $\hbar\mathbf{q}$ , excitations that carry a single unit of spin angular momentum. In turn, the plane-wave spectrum  $S_{\text{GG}'}^{+-}(\mathbf{q}, \omega)$  of a ferromagnet assumed spin polarized in the  $z$  direction encodes majority-to-minority magnons at positive frequencies and minority-to-majority magnons at negative frequencies. Concerning the reciprocal lattice vectors, it is useful to focus on the diagonal  $S_{\mathbf{G}}^{+-}(\mathbf{q}, \omega) = S_{\text{GG}}^{+-}(\mathbf{q}, \omega)$ . As the reciprocal lattice vector  $\mathbf{G}$  represents the local field component of the spin-flipping pair densities, it also represents the local spin texture of the excitations within the unit cell. Accordingly, the acoustic magnon mode will appear in the spectrum  $S_{\mathbf{G}}^{+-}(\mathbf{q}, \omega)$  for values of  $\mathbf{G}$  for which the magnetic atoms of the unit cell are in phase. Likewise, the optical mode of MnBi will be visible in  $S_{\mathbf{G}}^{+-}(\mathbf{q}, \omega)$  for values of  $\mathbf{G}$ , for which the two Mn atoms in the unit cell are out of phase.

## III. METHODOLOGY

### A. Ground-state Hubbard correction

Although one would not normally expect strong correlation effects in metals, previous *ab initio* studies of MnBi have shown that the LDA provides an insufficient description of properties ranging from lattice constants and equilibrium magnetic moments to the temperature-dependent magnetic anisotropy and magneto-optical effects [56,57]. For these properties, a significant improvement is obtained when including a Hubbard-type onsite correction to the  $3d$  electronic orbitals of Mn. In this study, we apply the rotationally invariant Dudarev LDA +  $U$  scheme [55], where the Coulomb interaction amongst the  $3d$  electrons is corrected with a single effective Hubbard parameter  $U_{\text{eff}} = U - J$ . The Hubbard



correction favors idempotency and splits the localized majority and minority  $3d$  bands by a value similar to  $U_{\text{eff}}$ .

## B. Hubbard correction and LR-TDDFT

In order to relate the Kohn-Sham susceptibility to the many-body susceptibility by means of the Dyson equation (5), the exchange-correlation (xc) kernel needs to be derived from a time-dependent xc potential that reproduces the correct ground-state spin densities and effective potentials in the static limit (in the absence of an external perturbation). This implies that the ALDA xc kernel cannot be used to calculate the transverse magnetic susceptibility based on a LDA +  $U$  ground-state calculation.

### 1. Collective enhancement

To elaborate on how the Dyson equation (5) breaks down in practice, we invert it in the plane-wave basis,

$$\chi_{[\mathbf{G}]}^{+-}(\mathbf{q}, \omega) = (1 - \chi_{\text{KS}}^{+-}(\mathbf{q}, \omega) f_{\text{LDA}}^{-+})_{[\mathbf{G}]}^{-1} \chi_{\text{KS}, [\mathbf{G}]}^{+-}(\mathbf{q}, \omega), \quad (10)$$

and compare it to the Dyson equation for a homogeneous electron gas (HEG), for which the susceptibility in reciprocal space is a scalar function of the wave number  $q$  [52,63]:

$$\chi^{+-}(q, \omega) = \frac{\chi_{\text{KS}}^{+-}(q, \omega)}{1 - \chi_{\text{KS}}^{+-}(q, \omega) f_{\text{LDA}}^{-+}}. \quad (11)$$

For  $\chi^{+-}(q, \omega)$ ,  $\chi_{\text{KS}}^{+-}(q, \omega)$  and the diagonal elements of  $\chi_{\text{GG}}^{+-}(\mathbf{q}, \omega)$ , the spectrum of induced excitations is proportional to the imaginary part of the susceptibility [47]:  $S_{\mathbf{G}}^{+-}(\mathbf{q}, \omega) = -\text{Im}[\chi_{\text{GG}}^{+-}(\mathbf{q}, \omega)]/\pi$ . The Kohn-Sham spectrum  $S_{\text{KS}}^{+-}(q, \omega)$  forms a continuum of Stoner pair excitations, that is, single-particle electron-hole pairs involving a single spin flip. Through Eq. (11), the Stoner excitations are carried over to the many-body spectrum  $S^{+-}(q, \omega)$  at a renormalized spectral intensity determined by the real part of the denominator. Apart from the Stoner excitations, Eq. (11) also permits a new type of excitation at the roots of the real part of the denominator. Inspired by this fact, we introduce the inverse enhancement function (IEF):

$$\kappa^{+-}(q, \omega) \equiv \text{Re} \left[ \frac{\chi_{\text{KS}}^{+-}(q, \omega)}{\chi^{+-}(q, \omega)} \right] = 1 - \text{Re}[\chi_{\text{KS}}^{+-}(q, \omega) f_{\text{LDA}}^{-+}]. \quad (12)$$

This function determines the collective enhancement of the many-body spectrum due to the electron-electron interaction described by  $f_{\text{LDA}}^{-+}$ . Outside the Stoner continuum, where  $\text{Im}[\chi_{\text{KS}}^{+-}(q, \omega)] = 0$ , collective magnon excitations appear at roots of the IEF. Furthermore, if the IEF vanishes (or nearly vanishes) inside the Stoner continuum, the Stoner pair excitations in the vicinity are enhanced. Whereas the Stoner continuum for the spin-polarized HEG is gapped at  $q = 0$  by the exchange splitting energy  $\Delta_x$ , the many-body spectrum exhibits a so-called Goldstone magnon mode with  $\omega_{q=0} = 0$ . As the IEF defines the magnon dispersion exactly outside the Stoner continuum, the Goldstone theorem thus dictates that  $\kappa^{+-}(0, 0) = 0$  for the spin-polarized HEG. In a similar spirit, we may introduce the following expression as the inverse

enhancement function for periodic crystals:

$$\kappa_{\mathbf{G}}^{+-}(\mathbf{q}, \omega) \equiv \text{Re} \left[ \frac{\chi_{\text{KS}, \mathbf{GG}}^{+-}(\mathbf{q}, \omega)}{\chi_{\mathbf{GG}}^{+-}(\mathbf{q}, \omega)} \right]. \quad (13)$$

Whereas the IEF for the HEG determines the collective enhancement in the Dyson equation (11),  $\kappa_{\mathbf{G}}^{+-}(\mathbf{q}, \omega)$  provides a *post hoc characterization* of the enhancement. Nevertheless, we find that the magnon condition  $\kappa_{\mathbf{G}}^{+-}(\mathbf{q}, \omega) = 0$  provides a good approximation for the peak position of magnon excitations away from dense parts of the Stoner continuum for MnBi as well as for the simpler itinerant ferromagnets Fe, Ni, and Co. More generally, it is the matrix  $(1 - \chi_{\text{KS}}^{+-}(\mathbf{q}, \omega) f_{\text{LDA}}^{-+})_{[\mathbf{G}]}^{-1}$  that determines the enhancement in the Dyson equation (10). Thus, it is somewhat surprising that the collective enhancement can be effectively characterized using a scalar function for each local field component. We attribute this success to the fact that the definition in Eq. (13) involves the fully enhanced  $\chi_{\text{GG}}^{+-}(\mathbf{q}, \omega)$ , thus implicitly accounting for the contribution of all plane-wave components.

### 2. Gap error and rescaling of the ALDA kernel

In Fig. 1(a) the collective enhancement is illustrated for the Goldstone mode of MnBi at  $\mathbf{q} = \mathbf{0}$ , calculated using the ALDA kernel on the LDA ground state. The Kohn-Sham spectrum has a well-defined peak at 2.9 eV, corresponding to the LDA exchange splitting. At the Kohn-Sham peak position, the IEF exhibits a polelike feature with a shape that closely resembles  $\text{Re}[\chi_{\text{KS}, \mathbf{GG}}^{+-}(\mathbf{q}, \omega)]$ , which in turn forms a Kramers-Kronig pair with the Kohn-Sham spectrum. In this way, the plane-wave IEF behaves exactly as one would expect from the HEG, where  $\text{Re}[\chi_{\text{KS}}^{+-}(q, \omega)]$  carries all the frequency dependence in  $\kappa^{+-}(q, \omega)$ , as seen from Eq. (12). Far away from the Stoner continuum, the Kohn-Sham susceptibility vanishes and the IEF goes to unity. Because the IEF takes negative values for frequencies just below the exchange splitting energy, it also obtains a root below the Kohn-Sham peak, which in the macroscopic case ( $\mathbf{G} = \mathbf{0}$ ) gives rise to the acoustic (Goldstone) magnon mode. For the ALDA kernel applied to the the LDA ground state shown in Fig. 1(a), the acoustic magnon frequency goes to zero in the long-range limit, thus fulfilling the Goldstone theorem (at least within some tenths of meV using the applied computational parameters).

When applying the ALDA kernel to the LDA +  $U$  ground state, however, the Goldstone theorem is violated. As shown in Fig. 1(b), including a Hubbard correction of  $U_{\text{eff}} = 3$  eV increases the Kohn-Sham peak position to 6.2 eV, i.e., the effective exchange splitting increases by a value  $\simeq U_{\text{eff}}$ . However, the ALDA kernel does not change sufficiently to accommodate the increased exchange splitting, resulting in a gap error of  $\omega_{\Gamma} = 2.6$  eV. In the HEG limit, the ALDA kernel amounts to a scalar entity giving the effective interaction strength amongst the single-particle Stoner excitations. Furthermore, the HEG magnon spectrum consists of a single mode, i.e., only a unique root in  $\kappa^{+-}(q, \omega)$  corresponds to a collective excitation. Consequently, the Goldstone condition  $\kappa^{+-}(0, 0) = 0$  fixes the scalar ALDA kernel  $f_{\text{LDA}}^{-+}$  in Eq. (11). Conversely, if the Goldstone condition is violated, it is consistent with the ALDA to simply scale the value of  $f_{\text{LDA}}^{-+}$  to satisfy  $\kappa^{+-}(0, 0) = 0$ . In a similar spirit, we rescale

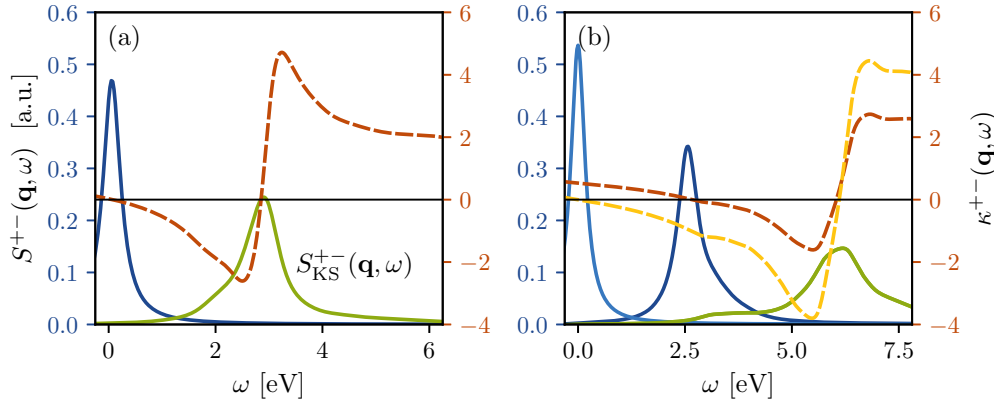


FIG. 1. Collective enhancement of the Goldstone mode in MnBi at  $\mathbf{q} = \mathbf{0}$ . The macroscopic Stoner spectrum  $S_{\text{KS}}^{+-}(\mathbf{q}, \omega) = S_{\text{KS}, \mathbf{G}=\mathbf{0}}^{+-}(\mathbf{q}, \omega)$  is shown in green, the inverse enhancement function  $\kappa_{\mathbf{G}=\mathbf{0}}^{+-}(\mathbf{q}, \omega)$  in red, and the macroscopic many-body spectrum  $S_{\mathbf{G}=\mathbf{0}}^{+-}(\mathbf{q}, \omega)$  in blue. (a) ALDA collective enhancement. (b) ALDA +  $U$  collective enhancement. Red and dark blue show the enhancement using the bare ALDA kernel calculated for the LDA +  $U$  ground state using  $U_{\text{eff}} = 3$  eV. The yellow and light blue colors show the enhancement using the  $\lambda$ ALDA +  $U$  kernel scaled to fulfill the Goldstone condition  $\kappa_{\mathbf{0}}^{+-}(\mathbf{0}, 0) = 0$ .

the plane-wave kernel  $f_{\text{LDA}, [\text{G}]}^{-+} \rightarrow \lambda f_{\text{LDA}, [\text{G}]}^{-+}$  such as to satisfy the approximate Goldstone condition  $\kappa_{\mathbf{G}=\mathbf{0}}^{+-}(\mathbf{q} = \mathbf{0}, \omega = 0) = 0$  whenever a Hubbard correction has been applied. Henceforward, we will refer to the kernel calculated in this way as the  $\lambda$ ALDA +  $U$  kernel. As seen in Fig. 1(b), this rescaling increases the intensity of the polelike feature in  $\kappa_{\mathbf{G}}^{+-}(\mathbf{q}, \omega)$  stemming from the Stoner continuum and thus effectively moves the root as well as the magnon peak position to zero frequency. Since the Hubbard correction mainly affects the  $3d$  electrons, it is a somewhat naive approach to rescale the entire ALDA kernel, but as we will show in Sec. IV B, the inclusion of a Hubbard correction in the  $\lambda$ ALDA +  $U$  approach leads to significant improvements of the magnon dispersion when compared to experiment. As a result, it seems that the  $\lambda$ ALDA +  $U$  approach can be a valuable tool for including correlation effects within LR-TDDFT in a simple and transparent way. In the literature, more advanced approaches have been developed to reclaim the self-consistency between the exchange-correlation kernel and Kohn-Sham susceptibility in order to strictly satisfy the Goldstone theorem, also when it is violated due to numerical limitations [41–43]. For a broader application of the LR-TDDFT methodology within, e.g., the transition metal pnictide family, it would be of high interest to make a comparative study of different strategies to satisfy the Goldstone condition in calculations with Hubbard corrections in the ground state.

Analogously to the  $\lambda$ ALDA +  $U$  approach, a global rescaling of the effective interaction has also previously been applied to satisfy the Goldstone theorem in MBPT calculations of the magnon dispersion [50,51]. Based on the  $GW$  approximation for the self-energy and a static limit of the random phase approximation for the screened Coulomb potential  $W$ , one may rescale  $W \rightarrow \lambda W$  to satisfy the Goldstone theorem when using the LDA +  $U$  Green's function  $G_0$ . This approach leads to an improved magnon stiffness for fcc Ni as compared to a LDA-based calculation [50]. However, for fcc Ni the exchange splitting is overestimated already in the LDA and inclusion of the Hubbard correction worsens the overall magnon bandwidth (and thus the short-range transverse spin

correlations), contrary to the present case for MnBi. In MBPT, the justification for using a global rescaling of the effective interaction rests on similar grounds as in the  $\lambda$ ALDA +  $U$  approach (see, e.g., the comparison to the one-band Hubbard model presented in Ref. [58]). There is an important distinction, however: Even when using the LDA Kohn-Sham susceptibility as a starting point, a gap error is obtained in MBPT, due to the inconsistency with the  $GW$  self-energy approximation [58].

### C. Computational details

All calculations in this study have been carried out using the open-source GPAW code [64,65], with which the plane-wave susceptibility  $\chi_{\text{GG}'}^{+-}(\mathbf{q}, \omega)$  can be computed within LR-TDDFT [47]. In principle, the PAW implementation yields all-electron accuracy, but in practice it is not possible to construct a complete basis of projector functions. In the applied projector augmented wave (PAW) setups, only the Mn  $4s$  and  $3d$  as well as the Bi  $6s$ ,  $6p$ , and  $5d$  orbitals are included as valence states in the band summation of Eq. (4). In addition to the valence states, eight empty shell bands per atom are included as well. Furthermore, a (30, 30, 18)  $\Gamma$ -centered Monkhorst-Pack (MP) grid is used along with a plane-wave cutoff of 750 eV for the plane-wave basis in Eq. (10). These parameters were chosen based on an extensive convergence study of the magnon dispersion in the itinerant ferromagnets Fe, Ni, and Co [47] and we have checked that these parameters lead to well-converged results for MnBi as well.

Calculations have been carried out in the NiAs-type crystal structure, using the experimental room-temperature lattice constants ( $a = 4.287$  Å,  $c = 6.117$  Å) for LR-TDDFT calculations. It should be noted that the reference inelastic neutron scattering data available are taken at 5 K [21] and that the MnBi structure is contracting when cooling, all the way from 293 K, through the structural phase transition at 90 K, down to at least 20 K [16]. Nevertheless, we expect a fair comparison between theory and experiment, when using the room-temperature crystal structure for the simulations. Occasional comparisons of magnon dispersion relations with

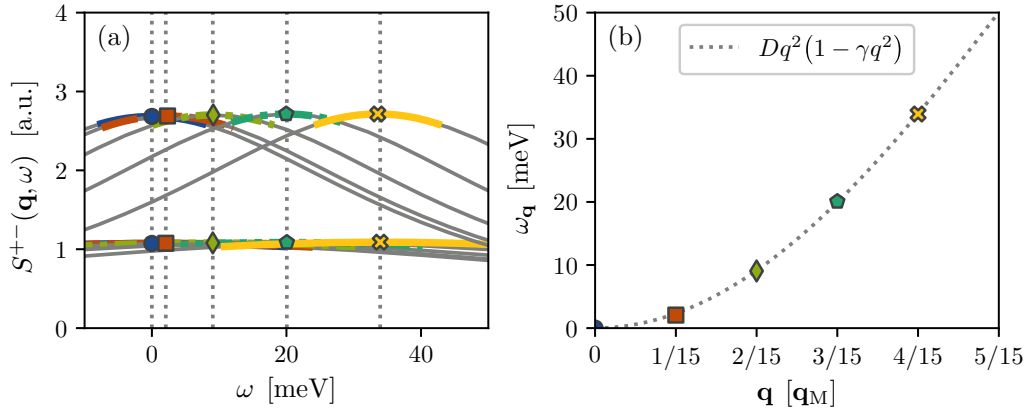


FIG. 2. Extraction of the magnon stiffness from the  $\lambda$ ALDA +  $U$  transverse magnetic excitation spectrum with  $U_{\text{eff}} = 3$  eV. (a) Magnon spectrum along the  $\Gamma \rightarrow M$  path calculated on a (30, 30, 18)  $\Gamma$ -centered MP grid using  $\eta = 100$  meV (lower set of line shapes) and a (60, 60, 36)  $\Gamma$ -centered MP grid using  $\eta = 40$  meV (upper set of line shapes). Magnon energies (scatter points) are identified as peak positions from a quadratic fit to the maximum of each Lorentzian line shape (colored lines). Vertical dotted lines indicate the magnon energies from the sparse  $k$ -point grid for visual comparison. (b) Extracted magnon dispersion from the calculation using the sparse  $k$ -point grid along with a biquadratic fit  $\omega_{\mathbf{q}} = Dq^2(1 - \gamma q^2)$ , to the dispersion.

calculations performed in the orthorhombic crystal structure reported at 80 K [16] have been carried out, without any noteworthy qualitative differences as a result.

In order to reliably extract the magnon dispersion, the Kohn-Sham continuum, which is sampled on a finite  $k$ -point mesh, needs to be broadened into a continuum. In practice this is done by leaving  $\eta$  as a small, but finite, parameter in Eq. (4). Through the average frequency displacement technique described in [47], it was found that the low-frequency Kohn-Sham spectrum of MnBi is effectively broadened into a continuum for values of  $\eta \geq 100$  meV using the chosen  $k$ -point grid. Unfortunately, the broadening parameter  $\eta$  not only dictates the minimum width of features in the Kohn-Sham spectrum, but in the many-body spectrum as well. Using  $\eta = 100$  meV, the spectral width of the magnons will be of the same order of magnitude as the MnBi magnon bandwidth. Consequently, it becomes difficult for the human eye to discern the magnon dispersion directly from the spectrum, as illustrated in Fig. 2(a), and it is not possible to extract a physical line shape for the magnons. This means that the Landau damping of the MnBi magnon modes cannot be studied with the present numerical resolution in GPAW. To elucidate such effects in MnBi, additional methodology would need to be implemented, such as the tetrahedron integration or analytic continuation techniques, which both previously have been proved effective for *ab initio* treatments of itinerant ferromagnets [41,52]. However, the available INS spectra do not exhibit any clear itinerant electron effects within the instrument resolution [21] and the study of such effects in MnBi is left for future work. Using the present methodology, we instead focus on the LR-TDDFT magnon dispersion, which includes magnon renormalization effects from the Stoner continuum in contrast to a Heisenberg model approach. To extract magnon energies, we sample the spectrum on a frequency grid with a spacing  $\delta\omega \leq \eta/8$  and compute the magnon frequency as the maximum in a parabolic fit to the magnon spectral peak. In Fig. 2(a), the magnon peak positions extracted from the (30, 30, 18)  $k$ -point grid are compared to similarly extracted

peak positions on a (60, 60, 36) grid, where it was possible to reduce  $\eta$  to a value of 40 meV without compromising the Kohn-Sham continuum. Clearly, it is not necessary to go beyond the (30, 30, 18)  $k$ -point grid in order to converge the magnon dispersion and a value of  $\eta = 100$  meV will be used throughout the remainder of the paper.

As a final note, we extract the magnon stiffness  $D$  along a given direction in reciprocal space by performing a biquadratic fit to the magnon peak positions of the four shortest  $\mathbf{q}$  vectors along the path in question (excluding the  $\Gamma$  point). This procedure is illustrated in Fig 2(b) for the  $\Gamma \rightarrow M$  direction.

## IV. RESULTS

### A. Correlation effects in the ground state

As argued in Refs. [56,57], it is necessary to include a Hubbard correction in the DFT ground-state description of MnBi in order to capture both structural and magnetic properties. In Fig. 3(a) we compare the lattice constants in the NiAs-type crystal structure calculated with LDA(+ $U$ ) to the experimental room-temperature crystal structure. Without a Hubbard correction, we find the lattice constants  $a = 4.131$  Å and  $c = 5.519$  Å, which are both underestimated compared to the experimental lattice constants at room temperature, differing by  $\Delta a = 0.156$  Å and  $\Delta c = 0.598$  Å, respectively. The temperature effect only provides a minor contribution to this difference. Experimentally,  $a$  and  $c$  are found to contract  $<0.02$  Å and  $<0.06$  Å, respectively, when the material is cooled from room temperature to 20 K [16]. Thus, the error mainly resides within the exchange-correlation functional, which in the case of LDA significantly underestimates the lattice constants, especially the out-of-plane lattice constant  $c$ , which determines the nearest-neighbor distance between the Mn atoms. In the case of LDA +  $U$ , however, reasonable lattice constants are obtained for values of  $U_{\text{eff}}$  within the range of 3–5 eV, with  $U_{\text{eff}} = 4$  eV providing the best match to experiment. In Fig. 3(b), we show the LDA(+ $U$ ) ground-state

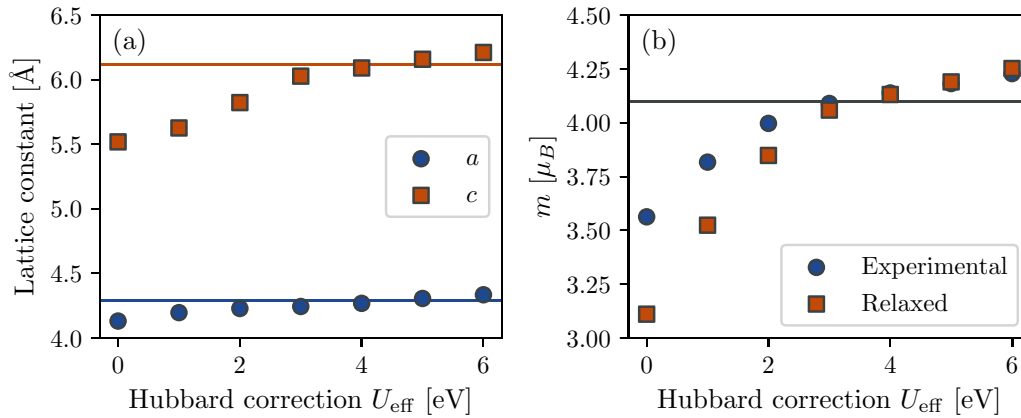


FIG. 3. Effects of Hubbard corrections on lattice parameters and magnetization. (a) LDA +  $U$  lattice constants as a function of  $U_{\text{eff}}$ , calculated using the atomic simulation recipes (ASR) [66]. Solid lines indicate the experimental lattice constants at room temperature [16]. (b) Magnetization per Mn atom as a function of  $U_{\text{eff}}$  using the experimental and LDA +  $U$  crystal structures, respectively. The experimental magnetization at 5 K [16] is shown as a reference.

magnetization per Mn atom calculated for the experimental and relaxed DFT crystal structures, respectively. In LDA, the magnetization is significantly underestimated with a value of  $3.56 \mu_B$  (to be compared with the experimental value of  $4.1 \mu_B$  [16]). If we instead use the LDA lattice constants, the situation is even worse as the magnetization takes a value of  $3.11 \mu_B$ . Again, this deficiency is amended upon the inclusion of a Hubbard correction and a reasonable agreement with experiment is found for values of  $U_{\text{eff}}$  in the range of 2–5 eV. As an alternative to Hubbard corrections, one can also obtain consistent improvements of ground-state properties using a generalized gradient approximation (GGA) functional [57]. However, whereas the GGA in-plane lattice constant matches experiments well, Hubbard corrections are still needed in order to capture the out-of-plane lattice constant and the magnetization. Similar to the lattice constant  $c$  in Fig. 3(a), the magnetization in Fig. 3(b) increases monotonically with  $U_{\text{eff}}$ , but most rapidly so for values of  $U_{\text{eff}}$  up to 3 eV. This can be understood based on the band structures and projected density of states shown in Fig. 4. Generally speaking, the Hubbard correction increases the exchange splitting, moving the minority bands up in energy and the majority bands down in energy compared to the Fermi level, hence the monotonic increase in magnetization. For the Kohn-Sham band structure in the vicinity of the Fermi level, one may separate the bands into two groups based on the orbital projections. There is a group of narrow bands consisting mainly of Mn  $3d$  orbitals as well as a group of more dispersive bands of mixed orbital character. Due to the nature of the Hubbard correction, it mostly affects the narrow Mn  $3d$  bands. For  $U_{\text{eff}} = 3$  eV, the Mn  $3d$  minority bands are moved  $\sim 1$  eV up and the Mn  $3d$  majority bands are moved  $\sim 2$  eV down in energy with respect to the Fermi level. That is, the Mn  $3d$  exchange splitting is increased by a value  $\sim U_{\text{eff}}$ . For the Mn  $3d$  majority bands, the energy shift is not associated with a change in the occupancies, as the bands are placed 2–4 eV below the Fermi level in the LDA band structure. In contrast, there are Mn  $3d$  minority states situated around the Fermi level of the LDA band structure, some of them partially occupied. Since the Hubbard correction increases the exchange splitting, the Mn  $3d$  minority

bands are shifted away from the Fermi level and become fully unoccupied at  $U_{\text{eff}} = 3$  eV. Thus, for values of  $U_{\text{eff}}$  above 3 eV, the increasing magnetization is determined solely from the more dispersive bands of mixed orbital character, which are less affected by the correction. As a consequence, the magnetization increases only slowly with  $U_{\text{eff}}$  above 3 eV.

### B. Correlation effects in the magnon dynamics

While the effects of Hubbard corrections on the ground-state properties have been discussed in Refs. [56,57], we extend the discussion to include also the influence on the dynamic susceptibility of MnBi. As shown above, the LDA Kohn-Sham spectrum in Fig. 1(a) has a well-defined Stoner peak at 2.9 eV. From the band structure and projected density of states shown in Fig. 4(a), we see that the origin of this peak is the narrow Mn  $3d$  bands, which dominate the spin dynamics of the system as expected. However, as reflected in Fig. 4, the Fermi surface includes contributions from the dispersive bands of mixed orbital character and these will have an important influence on the fundamental spin excitations as well. As the exchange splitting between the Mn  $3d$  bands grows, a non-negligible contribution from the dispersive bands becomes visible below the main Stoner peak [see Fig. 1(b)]. For values of  $U_{\text{eff}}$  above 3 eV, it would be tempting to apply a localized (half-)integer spin model based on the gapped Mn  $3d$  bands, but this would largely neglect the itinerant electronic effects introduced by the dispersive bands crossing the Fermi level. For example, the magnon dispersion is expected to exhibit Landau damping, which originates from the coupling of the collective Mn  $d$ -band excitations to the Stoner continuum originating from states in the vicinity of the Fermi level. In contrast, LR-TDDFT includes contributions from all bands on the same footing and is expected to capture both the Landau damping as well as the associated renormalization of the magnon dispersion.

In Fig. 5, we show the experimental magnon spectrum as measured by inelastic neutron scattering on single-crystalline MnBi [21] and compare it to the theoretical magnon dispersion relations computed within LR-TDDFT. The magnon



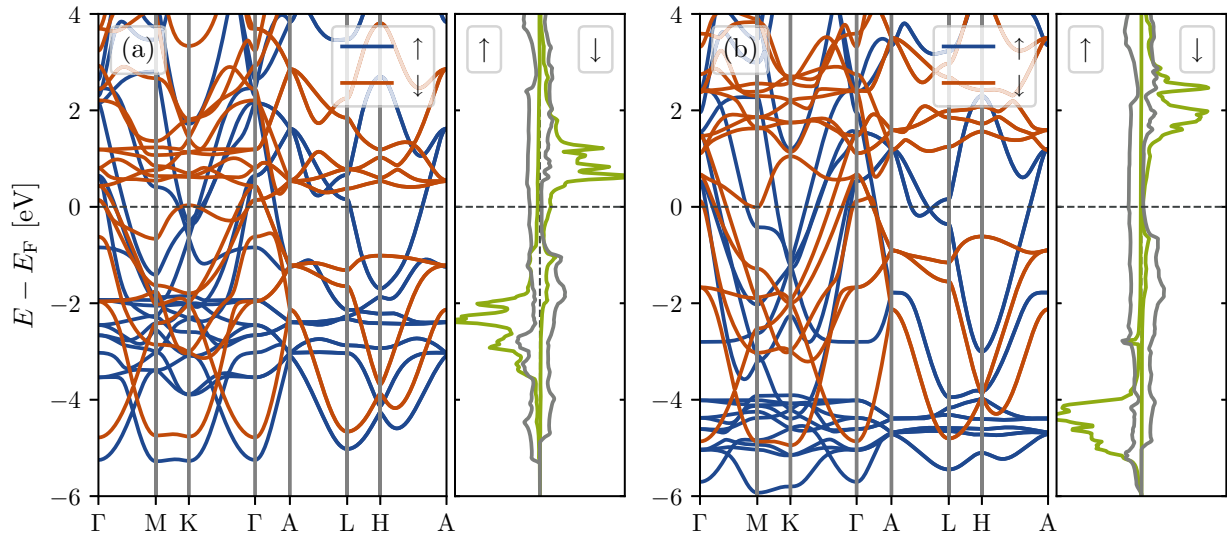


FIG. 4. Kohn-Sham electronic band structure and projected density of states (PDOS). Projections in green indicate the Mn 3d orbitals, whereas the gray projections show the sum of contributions from the Mn 4s, Mn 4p, Bi 6s, and Bi 6p orbitals. (a) LDA band structure and PDOS. (b) LDA +  $U$  band structure and PDOS ( $U_{\text{eff}} = 3$  eV).

dispersion is quite anisotropic, differing substantially between the in-plane ( $\Gamma \rightarrow M$ ) direction and the out-of-plane ( $\Gamma \rightarrow A$ ) direction. This difference arises, as the nearest-neighbor exchange interaction (which is out of plane) is strongly antiferromagnetic, while all other couplings are ferromagnetic. In order to fit the magnon spectrum to a Heisenberg model, it is necessary to include interactions up to the sixth-nearest neighbors (such that each Mn site is directly coupled to 40 other Mn sites), and even in this case, the magnon stiffness is underestimated in the model [21]. The long range of the exchange interactions is attributed the itinerant nature of MnBi and when calculating the magnon dispersion within

the ALDA (which is parameter free), we get a better match of the magnon stiffnesses (long-range magnon dispersion) to experiment than it is the case with the fitted Heisenberg model. However, the ALDA completely fails to describe the optical magnon mode both quantitatively and qualitatively. In Fig. 5, the optical mode can be observed around the reciprocal lattice vectors  $(0, 0, 1)$  and  $(1, 0, 1)$ , where the ALDA magnon frequencies are more than double compared to experiment. Furthermore, the experimental dispersion attains a minimum at the  $\Gamma$  point for the optical mode, most clearly seen at  $\mathbf{G} = (1, 0, 1)$ , whereas the ALDA dispersion attains a maximum. This shortcoming of the ALDA is to a large

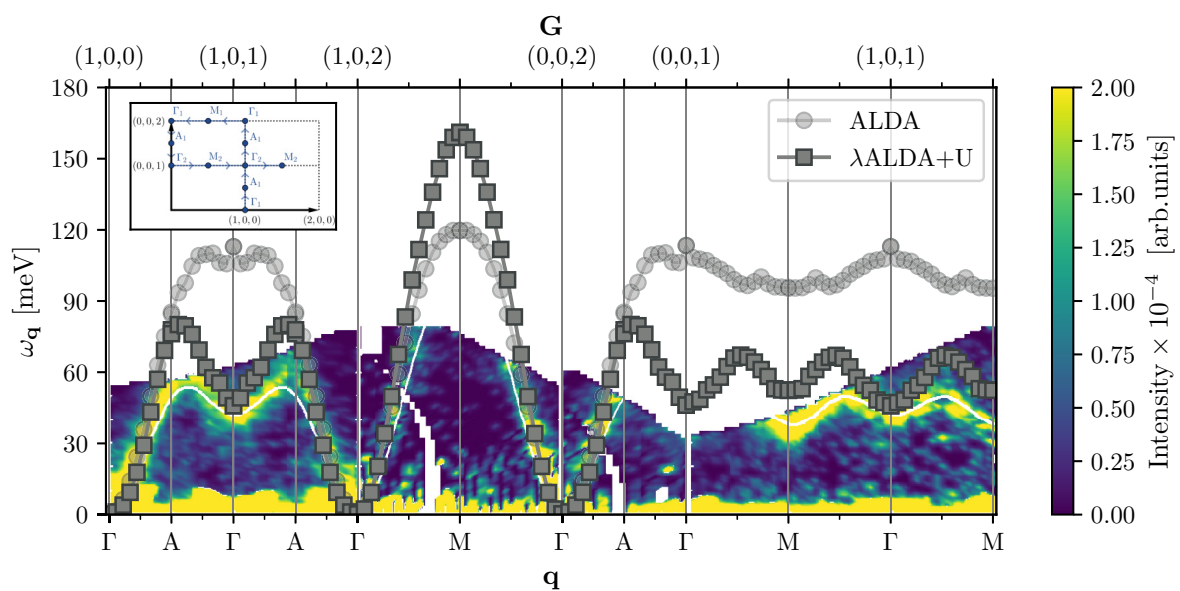


FIG. 5. Theoretical ALDA and  $\lambda$ ALDA +  $U$  ( $U_{\text{eff}} = 3$  eV) magnon dispersion relations plotted on top of a heat map of the transverse magnetic structure factor as probed by inelastic neutron scattering [21]. In the inset, the wave-vector path  $\mathbf{G} + \mathbf{q}$  is shown, given in coordinates of the reciprocal lattice vectors of the hexagonal NiAs crystal structure.

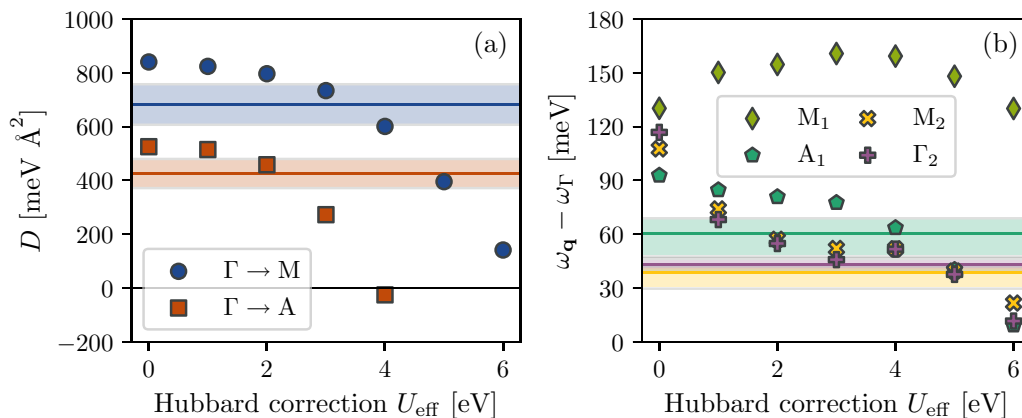


FIG. 6. MnBi magnon dispersion as a function of Hubbard  $U_{\text{eff}}$ . (a) Extracted magnon stiffness along the  $\Gamma \rightarrow M$  and  $\Gamma \rightarrow A$  directions. Horizontal lines and colored areas indicate the experimental best estimates and  $1\sigma$  uncertainty intervals of biquadratic fits to the transverse magnetic structure factor as probed by inelastic neutron scattering [21]. (b) Extracted magnon energies at a selected number of high-symmetry points. The experimentally determined magnon energies are shown by horizontal lines and the colored areas indicate their uncertainties.

extent amended by the inclusion of a Hubbard correction and both the acoustic and optical magnon modes agree reasonably well with the experimental spectrum within the  $\lambda\text{ALDA} + U$  approach with  $U_{\text{eff}} = 3$  eV. As the optical mode characterizes magnon excitations where the magnetization at neighboring Mn atoms (out of plane) precess out of phase, it seems that an appropriate description of static correlation effects is essential for capturing the short-range antiferromagnetic exchange interaction. At the same time, it is crucial to incorporate the itinerant nature of MnBi in order to capture the long-range ferromagnetic exchange interactions. This makes the inherent magnetic frustration of MnBi a highly nontrivial problem to treat theoretically. Therefore, it is a noteworthy achievement that we are able to reproduce the experimental magnon dispersion using a simple Hubbard correctional scheme within the framework of LR-TDDFT.

### C. Correlation effects and the Hubbard parameter

So far, we have presented excited-state quantities calculated using the effective Hubbard parameter  $U_{\text{eff}} = 3$  eV. However, the “correct” magnitude of the Hubbard correction cannot be uniquely defined, and in Fig. 6(a) we show the magnon stiffness as a function of  $U_{\text{eff}}$ . We have extracted the experimental magnon stiffness from a biquadratic fit to the inelastic neutron scattering data available [21], obtaining values  $D_M = 683 \pm 75$  meV  $\text{\AA}^2$  and  $D_A = 426 \pm 54$  meV  $\text{\AA}^2$  for the in-plane and out-of-plane magnon stiffnesses, respectively. Using the ALDA kernel, the magnon stiffnesses are slightly overestimated to values of  $D_M = 841$  meV  $\text{\AA}^2$  and  $D_A = 526$  meV  $\text{\AA}^2$ , clearly reproducing the stiffness anisotropy of experiment. Adding an increasing amount of Hubbard correction, as shown in Fig. 6(a), the magnon stiffness decreases along both directions, but more so in the out-of-plane direction than it does in plane. For the  $\Gamma \rightarrow A$  direction, the magnon stiffness reaches negative values for  $U_{\text{eff}} \geq 4$  eV, implying that the ferromagnetic ground state becomes dynamically unstable beyond this point, a fact which will be discussed in further detail below. Because the MnBi ground state is indeed ferromagnetic, this sets an upper bound on

appropriate values for  $U_{\text{eff}}$ . Overall, it seems that values of  $U_{\text{eff}} \leq 3$  eV provide a reasonable agreement with experiment for the magnon stiffnesses, with the best fit being somewhere in the range of 2–3 eV. As mentioned previously, it is especially the optical magnon frequencies, for which ALDA falls short. In Fig. 6(b) we show the magnon energy at the first BZ M point and A point,  $(1/2, 0, 0)$  and  $(0, 0, 1/2)$  in relative reciprocal coordinates, as well as the second BZ M point and  $\Gamma$  point,  $(1/2, 0, 1)$  and  $(0, 0, 1)$ , as a function of  $U_{\text{eff}}$ . Using the ALDA kernel, the magnon frequencies at the three high-symmetry points of the second BZ (this includes the A point) are significantly overestimated. Generally speaking, the three optical magnon frequencies decrease with increasing  $U_{\text{eff}}$ , coinciding with the experimental reference for separate values in the 3–5 eV range. However, it is not possible to obtain a complete simultaneous match to experiment of both magnon stiffnesses and optical magnon frequencies using the  $\lambda\text{ALDA} + U$  approach. From the results in Fig. 6, it seems that in order to reproduce the observed optical magnon frequencies as well as possible,  $U_{\text{eff}}$  should be chosen as large as the magnon stiffnesses permit.

Considering all the preceding results, ranging from lattice constants and magnetization to the magnon dispersion relation, it seems that a choice of  $U_{\text{eff}} \sim 3$  eV provides the best compromise between various material properties. This finding agrees quite well with the previous efforts of Antropov *et al.* to determine  $U$  and  $J$  [56]. Using the constrained local spin-density approximation (cLSDA) and constrained random phase approximation (cRPA) methods, they obtain values for  $U$  of 4.57 and 3.6 eV, respectively. As these methods generally tend to overestimate and underestimate, respectively, the value for  $U$ , the authors deem a value of  $U \sim 4$  eV the most appropriate choice, which along with the cLSDA value for  $J = 0.97$  eV gives  $U_{\text{eff}} = U - J \sim 3$  eV.

Finally, we return to the dynamic instability of the ferromagnetic ground state, which occurs for  $U_{\text{eff}} \geq 4$  eV. In Fig. 7(a) we show the magnon dispersion close to the  $\Gamma$  point for values of  $U_{\text{eff}}$  below, on, and above the onset of the instability. At the onset itself ( $U_{\text{eff}} \sim 4$  eV), the magnon stiffness vanishes and the dispersion becomes flat along the

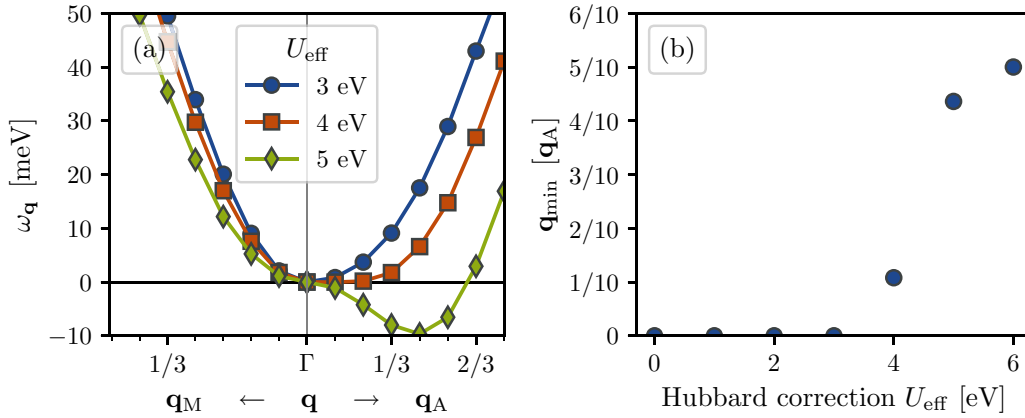


FIG. 7. (a) Magnon dispersion in the ferromagnetic state at different values for the Hubbard parameter  $U_{\text{eff}}$ . (b)  $\mathbf{q}$  point (in the  $\Gamma \rightarrow A$  direction) where the ferromagnetic magnon dispersion has its minimum as a function of the Hubbard parameter.

$\Gamma \rightarrow A$  direction, meaning that the low-frequency magnons disperse with some power larger than  $q^2$  in this direction. Above the onset, however, the magnon stiffness is finite and negative, such that the magnon dispersion attains its global minimum away from the  $\Gamma$  point and at negative magnon frequencies. This implies that a selection of magnon quasi-particle excitations with finite wave vectors  $\mathbf{q} \propto \mathbf{q}_A$  place the system in an energetically more favorable state than the ferromagnetic starting point, thus rendering the ferromagnetic state dynamically unstable. There is no reason to believe that the correlation effects included in the Hubbard correction quench magnetic order as a whole, rather they seem to enhance the nearest-neighbor exchange interaction, which is out of plane and antiferromagnetic. This is supported by calculations of the energy difference between the ferromagnetic state and the antiferromagnetic state with ferromagnetic alignment in plane and antiferromagnetic alignment out of plane. In Fig. 8 we illustrate the effective interlayer exchange coupling associated

with this energy difference, a coupling which is ferromagnetic, but of decreasing strength with increasing Hubbard correction  $U_{\text{eff}}$ . It should be stressed that this effective coupling strength is not a valid Heisenberg model parameter in its own right, rather it contains contributions from the exchange couplings at all length scales. Beyond the magnetic phase transition  $U_{\text{eff}} \geq 4$  eV, the (total) effective interlayer coupling is still ferromagnetic, and it seems likely that the new (hypothetical) ground state would be a helically ordered state. As a first estimate of the helical wave vector, we give in Fig. 7(b) the wave vector at which the ferromagnetic magnon frequency attains its minimum along the  $\Gamma \rightarrow A$  direction, determined from a fit to the  $\lambda\text{ALDA} + U$  dispersion using Gaussian process regression.

#### D. Hole doping and uniaxial compressive strain

Although the Hubbard parameter  $U_{\text{eff}}$  encodes real physical correlations in MnBi, it is not an actual parameter, which can be tuned in experiments. However, as previously hypothesized, the main role of the Hubbard correction regarding a possible phase transition to helical magnetic order seems to be that it enhances the nearest-neighbor antiferromagnetic exchange interaction to such an extent, that the ferromagnetic state becomes dynamically unstable. Whereas we cannot tune  $U_{\text{eff}}$  in real life, we can try to enhance the antiferromagnetic exchange and possibly realize a magnetic phase transition to helical order in this way. To this end, we investigate two different approaches: hole doping and uniaxial compressive strain. Investigating the effect of hole doping is motivated by the fact that Mn sits to the right of Cr in the periodic table. Cr is well known for exhibiting strong antiferromagnetic exchange interactions and by substituting a small amount of Mn with Cr it may be possible to induce a phase transition into a helically ordered ground state. Because large supercell LR-TDDFT computations currently are out of scope, we simulate this scenario by introducing holes into the electronic structure of MnBi (moving the Fermi level down). We do this with  $U_{\text{eff}}$  fixed to a value of 3 eV. The motivation for investigating strain effects on the magnon dynamics is more straightforward. If we can compress the nearest-neighbor bond length, the antiferromagnetic exchange interaction should be enhanced.

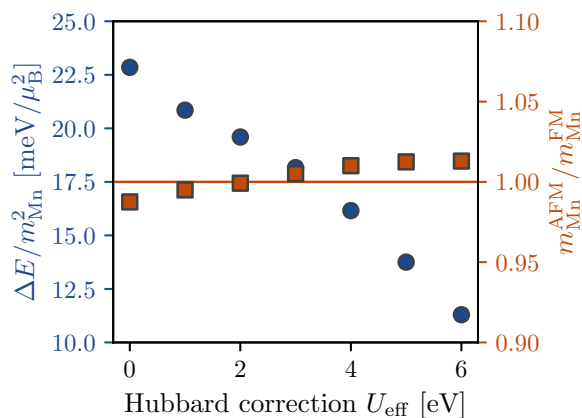


FIG. 8. LDA +  $U$  effective interlayer exchange coupling (left axis) between the in-plane layers of Mn atoms, given as a function of  $U_{\text{eff}}$ . The effective coupling is calculated from the energy difference per magnetic atom  $\Delta E = (E_{\text{Néel}} - E_{\text{FM}})/2$  and the average local moment on the Mn atoms  $m_{\text{Mn}} = (m_{\text{Mn}}^{\text{FM}} + m_{\text{Mn}}^{\text{Néel}})/2$  (within the PAW sphere of radius  $r_c = 2.1 a_0$ ). As a classical Heisenberg model picture of the interlayer coupling relies on the atomic spins being rigid, the relative sizes of the local Mn moments among the two states is shown on the right axis.

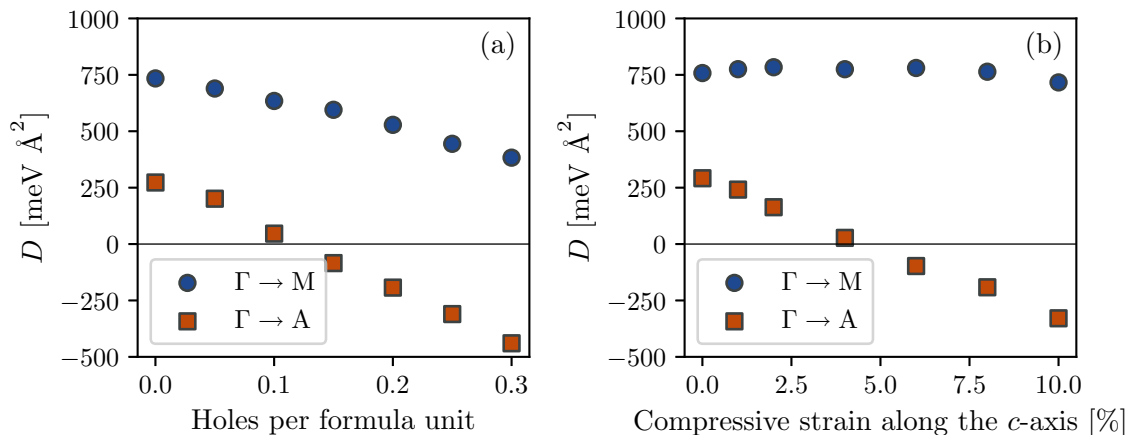


FIG. 9. Theoretical magnon stiffness along the  $\Gamma \rightarrow M$  and  $\Gamma \rightarrow A$  directions as (a) a function of removed electrons, (b) a function of uniaxial compressive strain in the  $c$  direction. Calculated with the  $\lambda$ ALDA +  $U$  kernel and  $U_{\text{eff}} = 3$  eV.

However, if we apply a hydrostatic pressure and reduce the crystal volume from all directions, also the ferromagnetic exchange interactions are expected to increase in strength. Thus, to simplify the picture, we compress the crystal along the  $c$  axis, while keeping the volume constant through an expansion of the in-plane lattice constant. In experiment, this would to some extent correspond to applying a uniaxial pressure. In Fig. 9, we show the magnon stiffness as a function of hole doping and uniaxial compressive strain. In both cases, the magnon stiffness decreases more or less linearly along the  $\Gamma \rightarrow A$  direction and the ferromagnetic state becomes unstable at 0.12 holes per formula unit and 4.4% compressive strain along the  $c$  axis (determined from linear interpolation). When hole doping the system, also the in-plane magnon stiffness along the  $\Gamma \rightarrow M$  direction decreases. This fits well with the intention of simulating a substitution of Mn with Cr, as one would also expect a weakening of the long-range ferromagnetic exchange interactions in this case. For the uniaxial compressive strain, it is less clear what to expect for the in-plane magnon stiffness. With the expansion of the in-plane lattice constant, the in-plane ferromagnetic exchange interactions are expected to become weaker, leading to a reduction in the frequency scale for  $D_M$ . At the same time, however, the length scale for  $D_M$  increases with an expanding  $a$  lattice constant. Seemingly, these opposite-sided effects cancel out, as the in-plane magnon stiffness in Fig. 9(b) is seen to be largely unaffected by the uniaxial compressive strain, at least for strains below 10% (which are really 5% strains in plane). The weakening of in-plane ferromagnetic exchange interactions is more clear from the in-plane magnon bandwidth (i.e., the magnon frequency at the first BZ M point), for which there is a decrease with *both* hole doping and uniaxial compressive strain, as seen in Fig. 10. In addition, also the magnon frequency in the A point decreases with both hole doping and uniaxial compressive strain. However, this is not the case for the second BZ M point and  $\Gamma$  point for which the magnon frequencies only decrease with strain. On the contrary, the magnon frequency in the second BZ center actually increases with hole doping. This is somewhat of a surprise since the second BZ  $\Gamma$ -point magnons correspond to spin-wave excitations where the nearest-neighbor Mn

atoms acquire opposite phases. Once again, this emphasizes that the magnetic frustration in MnBi is a highly nontrivial problem, due to the importance of static correlation effects and the fact that the long-range ferromagnetic exchange interactions cannot be boiled down to a simple set of short-range couplings.

Experimental studies have shown that it is indeed possible to dope MnBi with Cr, at least for thin films [18,19] and melt-spun ribbons [20]. It may even be an advantage for the synthesis to add Cr, as it helps to stabilize the formation of ferromagnetic MnBi as opposed to a decomposition into paramagnetic  $\text{Mn}_{1.08}\text{Bi}$  and Bi [20]. For both thin films and ribbons, the Curie temperatures of the investigated  $\text{Mn}_{1-x}\text{Cr}_x\text{Bi}$  alloys lie below the segregation temperature of 630 K. Based on these studies, it is not completely clear how the Curie temperature depends on Cr doping levels since the samples are rather inhomogeneous. As an example, the Cr content of the thin films was shown to depend on depth, with Cr concentrated at the surface [19]. With 10% Cr in the overall composition [comparable to the critical doping level for the helical phase transition according to the results of Fig. 9(a)], the Curie temperature was decreased to 523 and 546 K for the thin films and ribbons, respectively. The fact that Cr doping lowers the Curie temperature is in good agreement with our results, but a confirmation of the calculated trends and existence of a magnetic phase transition (possibly at low temperatures) requires further experimental studies. To our knowledge, it is an open question as to how MnBi behaves under uniaxial pressure. From the present theoretical investigations, it does not seem realistic to induce a phase transition to helical magnetic order in a uniaxial pressure cell, as one would expect the crystal to break long before obtaining a 4.4% uniaxial compressive strain. However, based on the fact that  $D_A$  decreases linearly with both hole doping and strain, as seen in Fig. 9, one could hope to combine the two effects, such that the hypothetical helical phase transition of the  $\text{Mn}_{1-x}\text{Cr}_x\text{Bi}$  alloys could be induced by pressure for Cr-doping levels close to the phase transition. Indeed, it seems that both effects produce similar trends for the minimal frequency magnon wave vectors beyond the magnetic phase transition, as seen in Fig. 11.



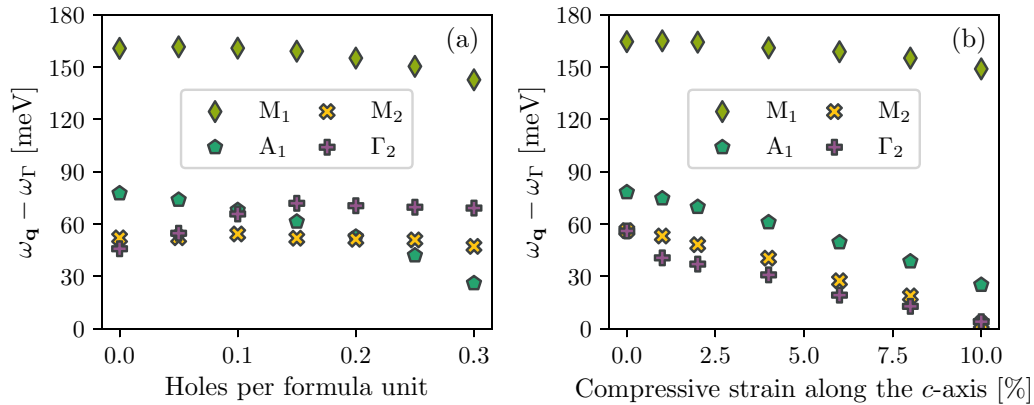


FIG. 10. Theoretical magnon energies at a selected number of high-symmetry points as (a) a function of removed electrons, (b) a function of uniaxial compressive strain in the  $c$  direction. Calculated with the  $\lambda$ ALDA +  $U$  kernel and  $U_{\text{eff}} = 3$  eV.

## V. DISCUSSION

In this paper, we have mainly discussed the magnon dynamics of pristine MnBi and Cr-doped alloys. However, the results can be regarded as an initial step in a broader context since many of the quantum magnetic phenomena studied here are shared by the family of transition metal pnictides. Among the Mn- and Cr-based compounds, helical magnetic order is quite common and the helical wave vectors have also previously been shown to depend on the relative concentrations of Mn and Cr [10]. As an example, the  $\text{Mn}_{1-x}\text{Cr}_x\text{As}$  phase diagram includes a phase transition from ferromagnetic MnAs to helically ordered CrAs [15]. In addition, MnP has been shown to exhibit pressure-induced magnetic phase transitions between ferromagnetic and helical order as well as pressure-induced superconductivity [10,13], which is also found in CrAs [14].

Also the inherent magnetic frustration in the transition metal pnictide family has been the subject of several previous studies. Based on analysis of the band structure and partial occupation of orbitals in MnP, Goodenough provided a qualitative explanation for the existence of both antiferromagnetic and ferromagnetic order at different temperatures [11]. He argued that the half-filling of the localized Mn  $t_{2g}$  orbital directed towards the nearest Mn neighbors calls for an anti-

ferromagnetic ordering while the three-fourths filling of the collective, yet narrow,  $3d$  bands representing the remaining  $t_{2g}$  orbitals calls for ferromagnetic ordering. Similar considerations have also been explored for MnAs, where exchange striction also plays a role in the competition between the NiAs and MnP structural phases [12].

In this context, the theoretical prediction that magnetic order in MnBi is characterized by a competition between nearest-neighbor antiferromagnetic exchange and long-range ferromagnetic exchange has some precedent, as similar effects have been observed in closely related members of the transition metal pnictide family. Similarly, it seems likely that the prediction of a phase transition to helical magnetic order in Cr-doped MnBi could be correct and that the phase transition would be strain sensitive.

The coupling between structural and magnetic degrees of freedom may also help to explain why the Hubbard correction has such a strong influence on the out-of-plane lattice constant  $c$ , as shown in Fig. 3(a). As the appropriate correlation effects are included with increasing  $U_{\text{eff}}$  and the antiferromagnetic exchange interaction between nearest neighbors is increased, it becomes favorable to increase the nearest-neighbor distance as a compensation for the ground-state remaining ferromagnetic. Similarly, a magnetic phase transition to helical order

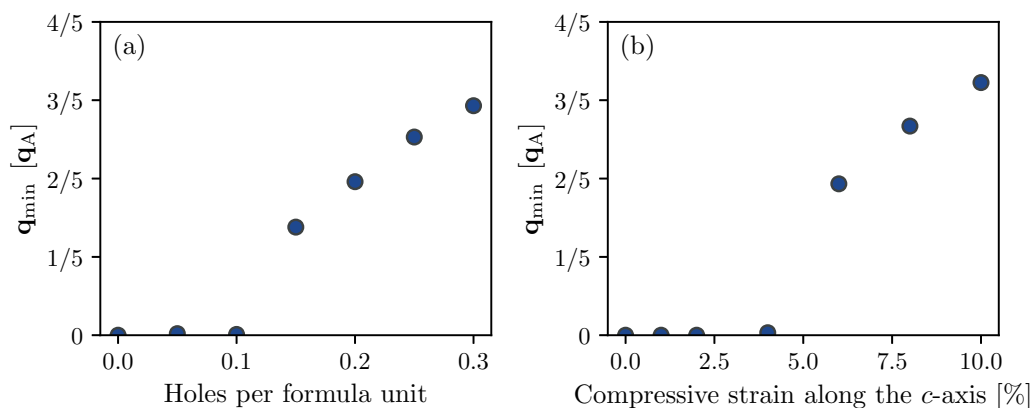


FIG. 11.  $\mathbf{q}$  point where the ferromagnetic magnon dispersion has its minimum along the  $\Gamma \rightarrow \text{A}$  path as (a) a function of removed electrons, (b) a function of uniaxial compressive strain in the  $c$  direction. Calculated with the  $\lambda$ ALDA +  $U$  kernel and  $U_{\text{eff}} = 3$  eV.

could be accompanied by a structural compression in the  $c$  direction, as the antiferromagnetic nearest-neighbor exchange interaction does no longer need to be compensated to the same extent. Another possibility is that MnBi undergoes a structural phase transition from the hexagonal NiAs structure into the orthorhombic MnP structure with Cr doping, as it is the case in the  $\text{Mn}_{1-x}\text{Cr}_x\text{As}$  phase diagram.

Although the occurrence of similar phenomena in other transition metal pnictides inspire confidence in the qualitative predictions made on the basis of this study, the quantitative predictions may depend somewhat on the details in the theoretical representation of doping and strain. The by-hand introduction of hole doping and uniaxial compressive strain should be viewed as efforts to study the underlying physical mechanisms and not to provide accurate estimates for, e.g., the critical Cr-doping level for the magnetic phase transition. Actually, the critical doping levels and strains for the phase transition are likely to be underestimated, as the Hubbard parameter  $U_{\text{eff}} = 3$  eV used here leads to an underestimate of the out-of-plane magnon stiffness  $D_A$ , as seen in Fig. 6(a). In this sense, the undoped and unstrained MnBi is closer to a helical phase transition in our simulations than the experiments predict (based on the magnon stiffness).

## VI. CONCLUSION

MnBi has a long history of experimental as well as theoretical investigations based on its attractive properties for technological applications. As we have shown in this study, MnBi exhibits a nontrivial inherent magnetic frustration, which makes it an intriguing subject for theoretical studies, but also implies a potential for future discovery of new magnetic phases. The nearest-neighbor exchange interactions between Mn  $3d$  electrons are strongly antiferromagnetic and highly susceptible to correlation effects, but despite the strength of these interactions, the ground-state magnetic order is determined by the long-range ferromagnetic exchange. Because the competing magnetic interactions arise from electrons of localized and itinerant character, respectively, it is a substantial theoretical challenge to provide an appropriate description of the magnetic frustration in MnBi.

In this study, we have shown that it is in fact possible to capture the magnetic frustration from the perspective of (LR-TD)DFT calculations, both for the ground-state properties of MnBi, but also for the magnon dynamics. The itinerant and localized correlations in MnBi have been described at the LDA +  $U$  level and for the LR-TDDFT calculations, we

utilize a scalar rescaling of the ALDA kernel based on considerations of the Goldstone criterion for the homogeneous electron gas. With the rescaled  $\lambda\text{ALDA} + U$  kernel, we are able to reproduce the experimental magnon dispersion using a Hubbard correction of  $U_{\text{eff}} = 3$  eV, which in turn also provides ground-state properties that are in accordance with experiment. In this way, this study may pave the way for future theoretical studies of magnon dynamics in the transition metal pnictide family. To this end, we hope that first-principles calculations can provide a new angle of insight into the wide range of phenomena driven by magnetic frustration and magnetic fluctuations.

With an *ab initio* description of the magnon dynamics of MnBi in place, we have explored some of the phenomena that arise from the magnetic frustration. We have shown that an increase of the local electronic correlations gives rise to a decrease in the magnon stiffness out of plane ( $D_A$ ) due to an increased strength of the antiferromagnetic exchange interactions between the nearest neighbors. At  $U_{\text{eff}} \sim 4$  eV, the magnon stiffness changes sign, meaning that a phase transition takes place, most likely in the favor of a phase of helical order. Whereas the increase in electronic correlations is an artificial one, we have shown that a similar increase in antiferromagnetic interaction strength may be imposed using hole doping or uniaxial compressive strain, in both cases leading to a similar phase transition. In particular, it seems realistic to realize this phase transition by substituting 10%–20% of the Mn content with Cr. Similarly, it may be possible to induce the transition by applying uniaxial pressure, but only for compositions of  $\text{Mn}_{1-x}\text{Cr}_x\text{Bi}$  close to the critical Cr-doping level. Furthermore, we predict the helical wave vector  $\mathbf{q}$  to be sensitive to the Cr-doping level and strain, especially for doping levels and strains close to the phase transition.

To further unravel the inherent magnetic frustration in MnBi, additional experiments on single-crystalline MnBi are highly desirable. Especially, investigations of the effect of Cr doping and a possible phase transition to helical magnetic order are of great interest. Such investigations could potentially provide an improved understanding of the physical mechanisms underlying a wide range of members in the family of transition metal pnictides.

## ACKNOWLEDGMENT

T.S. and T.O. acknowledge support from the Villum foundation Grant No. 00029378.

- 
- [1] E. Adams, W. M. Hubbard, and A. M. Syeles, *J. Appl. Phys.* **23**, 1207 (1952).
  - [2] J. B. Yang, K. Kamaraju, W. B. Yelon, W. J. James, Q. Cai, and A. Bollero, *Appl. Phys. Lett.* **79**, 1846 (2001).
  - [3] V. Ly, X. Wu, L. Smillie, T. Shoji, A. Kato, A. Manabe, and K. Suzuki, *J. Alloys Compd.* **615**, S285 (2014).
  - [4] B. W. Roberts, *Phys. Rev.* **104**, 607 (1956).
  - [5] H. J. Williams, R. C. Sherwood, and O. L. Boothby, *J. Appl. Phys.* **28**, 445 (1957).
  - [6] J. M. D. Coey, *IEEE Trans. Magn.* **47**, 4671 (2011).
  - [7] G. Di, S. Iwata, S. Tsunashima, and S. Uchiyama, *J. Magn. Magn. Mater.* **104-107**, 1023 (1992).
  - [8] H. J. Williams, R. C. Sherwood, F. G. Foster, and E. M. Kelley, *J. Appl. Phys.* **28**, 1181 (1957).
  - [9] Di Chen, G. Otto, and F. Schmit, *IEEE Trans. Magn.* **9**, 66 (1973).
  - [10] Y. Wang, Y. Feng, J.-G. Cheng, W. Wu, J. L. Luo, and T. F. Rosenbaum, *Nat. Commun.* **7**, 13037 (2016).

- [11] J. B. Goodenough, *J. Appl. Phys.* **35**, 1083 (1964).
- [12] J. B. Goodenough and J. A. Kafalas, *Phys. Rev.* **157**, 389 (1967).
- [13] J.-G. Cheng, K. Matsubayashi, W. Wu, J. P. Sun, F. K. Lin, J. L. Luo, and Y. Uwatoko, *Phys. Rev. Lett.* **114**, 117001 (2015).
- [14] W. Wu, J. Cheng, K. Matsubayashi, P. Kong, F. Lin, C. Jin, N. Wang, Y. Uwatoko, and J. Luo, *Nat. Commun.* **5**, 5508 (2014).
- [15] J. Luo and J. Cheng, *J. Phys.: Condens. Matter* **29**, 440301 (2017).
- [16] M. A. McGuire, H. Cao, B. C. Chakoumakos, and B. C. Sales, *Phys. Rev. B* **90**, 174425 (2014).
- [17] T. Chen, *J. Appl. Phys.* **45**, 2358 (1974).
- [18] P. R. Bandaru, T. D. Sands, Y. Kubota, and E. E. Marinero, *Appl. Phys. Lett.* **72**, 2337 (1998).
- [19] P. R. Bandaru, T. D. Sands, D. Weller, and E. E. Marinero, *J. Appl. Phys.* **86**, 1596 (1999).
- [20] K. Anand, N. Christopher, and N. Singh, *Appl. Phys. A* **125**, 870 (2019).
- [21] T. J. Williams, A. E. Taylor, A. D. Christianson, S. E. Hahn, R. S. Fishman, D. S. Parker, M. A. McGuire, B. C. Sales, and M. D. Lumsden, *Appl. Phys. Lett.* **108**, 192403 (2016).
- [22] H. Xiang, C. Lee, H.-J. Koo, X. Gong, and M.-H. Whangbo, *Dalton Trans.* **42**, 823 (2013).
- [23] T. Olsen, *Phys. Rev. B* **96**, 125143 (2017).
- [24] D. Torelli and T. Olsen, *J. Phys.: Condens. Matter* **32**, 335802 (2020).
- [25] M. Pajda, J. Kudrnovský, I. Turek, V. Drchal, and P. Bruno, *Phys. Rev. B* **64**, 174402 (2001).
- [26] A. Liechtenstein, M. Katsnelson, V. Antropov, and V. Gubanov, *J. Magn. Magn. Mater.* **67**, 65 (1987).
- [27] P. Bruno, *Phys. Rev. Lett.* **90**, 087205 (2003).
- [28] M. I. Katsnelson and A. I. Liechtenstein, *J. Phys.: Condens. Matter* **16**, 7439 (2004).
- [29] Q. Niu and L. Kleinman, *Phys. Rev. Lett.* **80**, 2205 (1998).
- [30] R. Gebauer and S. Baroni, *Phys. Rev. B* **61**, R6459 (2000).
- [31] Z. Qian and G. Vignale, *Phys. Rev. Lett.* **88**, 056404 (2002).
- [32] D. M. Bylander, Q. Niu, and L. Kleinman, *Phys. Rev. B* **61**, R11875 (2000).
- [33] O. Grotheer, C. Ederer, and M. Fähnle, *Phys. Rev. B* **63**, 100401(R) (2001).
- [34] S. V. Halilov, H. Eschrig, A. Y. Perlov, and P. M. Oppeneer, *Phys. Rev. B* **58**, 293 (1998).
- [35] Q. Niu, X. Wang, L. Kleinman, W.-M. Liu, D. M. C. Nicholson, and G. M. Stocks, *Phys. Rev. Lett.* **83**, 207 (1999).
- [36] M. I. Katsnelson and A. I. Liechtenstein, *Phys. Rev. B* **61**, 8906 (2000).
- [37] R. B. Muniz and D. L. Mills, *Phys. Rev. B* **66**, 174417 (2002).
- [38] E. Runge and E. K. U. Gross, *Phys. Rev. Lett.* **52**, 997 (1984).
- [39] E. K. U. Gross and W. Kohn, *Phys. Rev. Lett.* **55**, 2850 (1985).
- [40] S. Y. Savrasov, *Phys. Rev. Lett.* **81**, 2570 (1998).
- [41] P. Buczek, A. Ernst, and L. M. Sandratskii, *Phys. Rev. B* **84**, 174418 (2011).
- [42] S. Lounis, A. T. Costa, R. B. Muniz, and D. L. Mills, *Phys. Rev. B* **83**, 035109 (2011).
- [43] B. Rousseau, A. Eiguren, and A. Bergara, *Phys. Rev. B* **85**, 054305 (2012).
- [44] N. Singh, P. Elliott, T. Nautiyal, J. K. Dewhurst, and S. Sharma, *Phys. Rev. B* **99**, 035151 (2019).
- [45] K. Cao, H. Lambert, P. G. Radaelli, and F. Giustino, *Phys. Rev. B* **97**, 024420 (2018).
- [46] N. Tancogne-Dejean, F. G. Eich, and A. Rubio, *J. Chem. Theory Comput.* **16**, 1007 (2020).
- [47] T. Skovhus and T. Olsen, *Phys. Rev. B* **103**, 245110 (2021).
- [48] F. Aryasetiawan and K. Karlsson, *Phys. Rev. B* **60**, 7419 (1999).
- [49] K. Karlsson and F. Aryasetiawan, *Phys. Rev. B* **62**, 3006 (2000).
- [50] E. Şaşıoğlu, A. Schindlmayr, C. Friedrich, F. Freimuth, and S. Blügel, *Phys. Rev. B* **81**, 054434 (2010).
- [51] H. Okumura, K. Sato, and T. Kotani, *Phys. Rev. B* **100**, 054419 (2019).
- [52] C. Friedrich, M. C. T. D. Müller, and S. Blügel, in *Handbook of Materials Modeling: Methods: Theory and Modeling*, edited by W. Andreoni and S. Yip (Springer, Cham, 2020), pp. 919–956
- [53] V. I. Anisimov, J. Zaanen, and O. K. Andersen, *Phys. Rev. B* **44**, 943 (1991).
- [54] A. I. Liechtenstein, V. I. Anisimov, and J. Zaanen, *Phys. Rev. B* **52**, R5467 (1995).
- [55] S. L. Dudarev, G. A. Botton, S. Y. Savrasov, C. J. Humphreys, and A. P. Sutton, *Phys. Rev. B* **57**, 1505 (1998).
- [56] V. P. Antropov, V. N. Antonov, L. V. Bekenov, A. Kutepov, and G. Kotliar, *Phys. Rev. B* **90**, 054404 (2014).
- [57] K. V. Shanavas, D. Parker, and D. J. Singh, *Sci. Rep.* **4**, 7222 (2015).
- [58] M. C. T. D. Müller, C. Friedrich, and S. Blügel, *Phys. Rev. B* **94**, 064433 (2016).
- [59] P. Hohenberg and W. Kohn, *Phys. Rev.* **136**, B864 (1964).
- [60] W. Kohn and L. J. Sham, *Phys. Rev.* **140**, A1133 (1965).
- [61] U. von Barth and L. Hedin, *J. Phys. C: Solid State Phys.* **5**, 1629 (1972).
- [62] A. K. Rajagopal and J. Callaway, *Phys. Rev. B* **7**, 1912 (1973).
- [63] M. Niesert, *Ab initio* calculations of spin-wave spectra from time-dependent density-functional theory, Ph.D. thesis, RWTH Aachen University, 2011.
- [64] J. J. Mortensen, L. B. Hansen, and K. W. Jacobsen, *Phys. Rev. B* **71**, 035109 (2005).
- [65] J. Enkovaara, C. Rostgaard, J. J. Mortensen, J. Chen, M. Duřak, L. Ferrighi, J. Gavnholt, C. Glinsvad, V. Haikola, H. a. Hansen, H. H. Kristoffersen, M. Kuisma, A. H. Larsen, L. Lehtovaara, M. Ljungberg, O. Lopez-Acevedo, P. G. Moses, J. Ojanen, T. Olsen, V. Petzold *et al.*, *J. Phys.: Condens. Matter* **22**, 253202 (2010).
- [66] M. Gjerding, T. Skovhus, A. Rasmussen, F. Bertoldo, A. H. Larsen, J. J. Mortensen, and K. S. Thygesen, *Comput. Mater. Sci.* **199**, 110731 (2021).